SAND2016-4391C

Three-Dimensional Measurement of Edge Effects in Open Cavities of Finite-Span

Edward P. DeMauro* Steven J. Beresh† Justin L. Wagner‡ John F. Henfling § and Russell W. Spillers¶

Sandia National Laboratories, Albuquerque, NM 87185, USA

Volumetric measurements of the flow within four open cavities were made using stereoscopic particle image velocimetry at a transonic freestream Mach number of 0.8. The cavities nominally had a length-to-diameter, $L/D = 7$, along with an aspect ratio, $b/L = 0.5$. The three complex cavity geometries were selected in order to model features representative of real aircraft bays and compare them to a finite-span rectangular cavity: these included features such as leading edge and side ramps, a scooped leading edge ramp, and a jagged leading edge. Flow is drawn into the cavity at the edges due to a lack of pressure recovery within the cavity. Due to the influence of the leading edge shape and side edges, three-dimensionalities are formed within the cavities that influence the development of the Rossiter tones. In the rectangular cavity, these three-dimensionalities lead to the formation of a set of counter-rotating streamwise-oriented vortices, which created a nearly-sinusoidal, spanwise waviness within its mixing layer. The addition of leading edge and side ramps disrupt the formation of these vortical structures and displace the mixing layer vertically, reducing Rossiter modal amplitudes. A scooped leading edge reintroduced streamwise vorticity, increasing cavity turbulence, whereas an overhanging jagged leading edge reduced cavity velocity fluctuations, while increasing the strength of the second Rossiter mode.

I. Introduction

Over the years there has been much interest in the flow over an open cavity, due to its applicability to aircraft bays. Flow separation at the leading edge of the cavity leads to a mixing layer that propagates downstream. The physical location of the mixing layer impingement on an inside surface of the cavity, dependent on the length-to-depth (L/D) ratio of the cavity, gives rise to one of three different cavity flow regimes: (1) *open* cavities ($L/D <$ 6-8), wherein impingement occurs on the rear cavity wall, leading to large-amplitude disturbances known as the Rossiter tones; (2) *closed* cavities ($L/D > 8$), wherein the mixing layer impinges on the floor of the cavity; (3) *transitional* cavities, which alternate between the two conditions.[1]

It has been shown within the literature that the Rossiter tones may be susceptible to three-dimensionalities. In particular, the presence of side walls are a non-negligible component of real-world aircraft bays that influence the cavity acoustics. Ahuja & Mendoza[2] showed that the amplitudes of the Rossiter tones were proportional to the aspect ratio (b/L) of the cavity. Disimile et al.[3] noted that the number of observable dominant frequencies within a cavity increased in proportion to aspect ratio, a finding echoed by Woo et al.[4] Hein et al.[5] reported increased acoustic radiation losses associated with three-dimensional cavities, in comparison to their two-dimensional counterparts. In addition to geometry, more recent studies have begun to highlight the possible influence of a spanwise, centrifugal instability associated with the recirculation vortex within the cavity.[6,7]

*Postdoctoral Appointee, Engineering Sciences Center, P.O. Box 5800, MS-0825, Albuquerque, NM 87125, AIAA Member. Corresponding author: epdemau@sandia.gov

†Distinguished Member of the Technical Staff, Engineering Sciences Center, P.O. Box 5800, MS-0825, Albuquerque, NM 87125, AIAA Associate Fellow.

‡Principle Member of the Technical Staff, Engineering Sciences Center, P.O. Box 5800, MS-0825, Albuquerque, NM 87125, AIAA Member.

§Principal Technologist

¶Senior Technologist

These changes to the cavity acoustics are related to physical three-dimensionalities that manifest within the cavity flow field, and their effect on the mixing layer. George et al.[8] reported that there was a vertical shift in the location of mixing layer impingement on the rear wall with decreasing aspect ratio. In addition to this, Sun et al.[9] observed a spanwise waviness present within the mixing layer of cavities with finite walls. This vertical shift and the spanwise wavy pattern are both due to the presence of spillage vortices, which are streamwise-oriented structures along the side edges of the cavity. These structures have been observed within the literature by a number of researchers.[2,10–15] Beresh et al.[11,12] showed the presence of increased turbulent kinetic energy near the rear corners of a finite cavity in both transonic and supersonic freestream conditions associated with the presence of these structures; in addition, Ohmichi & Suzuki[13] noted the existence of spillage vortices in hypersonic flow conditions. Work by Arunajatesan et al.[14] showed that the spanwise influence of the spillage vortices was dependent on the width of the cavity, resulting in either a net inflow or outflow at centerline, near the rear wall of the cavity. In addition, Crook et al.[15] used multiple PIV measurements to construct a diagram explaining the existence of all vorticity within a finite-span cavity in low-speed conditions, theorizing that the spillage vortices were two legs of a horseshoe vortex structure.

Other morphological changes may also effect alterations to the tonal frequencies and amplitudes. Wagner et al.[16] demonstrated the influence of a store on the acoustics of a rectangular cavity; in particular they saw a shift in modal frequencies and changes to the modal amplitudes. Of particular interest was the influence of the cavity tones on the store itself, where the store responded to streamwise and wall-normal disturbances at its natural frequencies. In contrast, simulations by Coley & Lofthouse[17] observed little alteration of the cavity tones, however they also noted structural resonance and a tendency for a store to enter into a pitch-up motion upon release.

Aside from the presence of a store, it is apparent that true aircraft bays have more complicated geometric features than represented by a simple rectangular cavity. A number of studies have been performed in order to study the effect of deployed doors on the cavity acoustics.[18–21] In addition to these, work by Casper et al.[22] has looked to address the influence of additional features such as ramps, variable L/D, and channels on the Rossiter tones. More recently, DeMauro et al.[23] showed evidence that, in the presence of a transonic freestream Mach number, side ramps suppress the formation of spillage vortices, altering the spanwise distribution of the time-averaged velocity field. In general, the studies cited here indicate that these features can lead to modification of the Rossiter tonal frequencies and amplitudes, and therefore warrant further investigation.

This study is a continuation of the work of Casper et al.[22] and DeMauro et al.,[23] which respectively investigated the acoustics and flow features associated with a set of complex geometries. These geometries, designed to more closely approximate a real-world aircraft bay, contain additional features such as ramps, channels, and a non-uniform leading edge. This work investigates how many of these features effect changes to the cavity flow field, in transonic freestream conditions. In particular, experiments were conducted in order to elucidate the physical differences present due to the influence of the various geometric features, with the hypothesis that the Rossiter tones are sensitive to streamwise vorticity and spanwise variation within the mixing layer.

II. Experimental Setup

Experiments were conducted at Sandia National Laboratories' Trisonic Wind Tunnel (TWT) facility, using a blowdown-to-atmosphere wind tunnel with a rectangular test section measuring 305 mm × 305 mm, enclosed within a pressurized plenum. To mitigate the effect of acoustic resonance due to the test section duct mode, porous walls were employed for the upper surface and a single side surface.[24] The experiments were performed at a freestream Mach number, $M_\infty = 0.8$; the stagnation pressure and temperature of the tunnel were held at constant values: $P_0 = 112$ kPa and $T_0 = 321 \pm 2$ K, respectively, with the test section walls at a temperature of 307 ± 3 K. These conditions corresponded to a freestream velocity of $U_\infty = 270.5$ m/s, measured at the entrance of the test section, resulting in an experimental Reynolds number of $\frac{Re_L}{L} = 18.9 \cdot 10^6$ m^{-1}.

The complex cavity hardware is formed from a simple rectangular cavity mounted such that its upper surface was flush with the tunnel floor. The dimensions of the rectangular cavity are $L = 203.2$ mm, $D = 29$ mm, and $b = 101.6$ mm, resulting in $L/D = 7$ and $b/L = 0.5$. The various complex geometries are modifications of this initial rectangular cavity, created by adding a number of different components to the front and side edges of the cavity (Fig. 1). These features are designed to approximate the flight geometry of

a realistic aircraft bay by adding non-uniformities to the incoming flow through the use of ramped surfaces. For ease of manufacturing, flat surfaces with angles were used instead of curved surfaces. Care was taken in the design of these ramped elements to ensure that angles were below limits for incipient separation.[22]

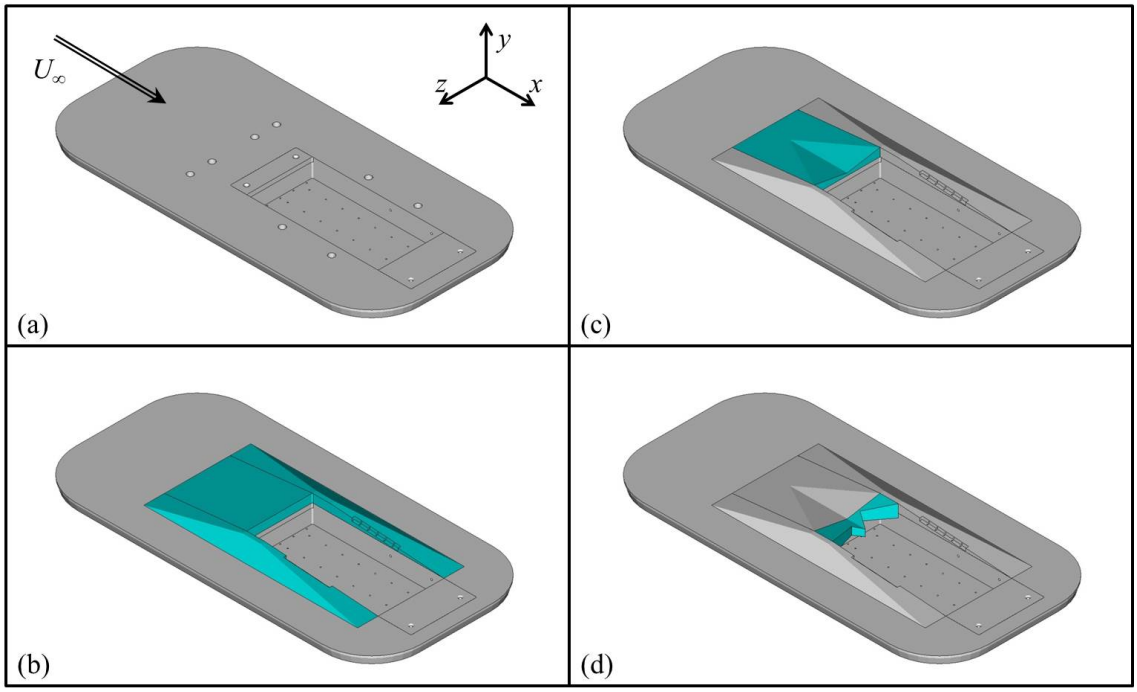

Figure 1. Geometric modification of the rectangular cavity resulting in the complex geometries tested: (a) rectangular cavity; (b) baseline complex cavity; (c) center scoop complex cavity; (d) center scoop & tooth (i.e. jagged leading edge overhang) complex cavity. Blue color indicates the feature added to make a given configuration.

The baseline complex cavity (Fig. 1b) is formed by the addition of a smooth ramp, inclined at an angle of 5.7°, which raises the leading edge of the cavity 12.7 mm above the trailing edge. Two side ramps are also added to the baseline complex cavity in order to provide for a smooth transition from this elevated leading edge to the trailing edge height. It should be noted here that the side ramps have angles of 26.6° in the spanwise direction. The baseline complex cavity, therefore has a streamwise variation in L/D with a value of 4.9 at its leading edge, decreasing to 7 at the trailing edge.

Modification of the leading edge ramp on the baseline complex cavity leads to the center scoop configuration (Fig. 1c). The purpose of the scoop is to approximate influence of the engine inlet on the oncoming flow over the cavity. As flow by-passes the engine inlet, it can travel down a shallow channel leading into the bay. Furthermore, this flow passes over a jagged leading edge that over-hangs into the weapons bay, which is modeled in the center scoop & tooth complex cavity (Fig. 1d). Table 1 lists the various geometries used in this study with their associated acronym. For the remainder of this paper, these cavities will be referred to by these acronyms.

Table 1. Complex Geometry Configurations

Configuration	Acronym	Side Ramps	Front Ramp	Tooth
Simple Rectangular	SR	No	No	No
Baseline Complex	BC	Yes	Smooth	No
Center Scoop Complex	CS	Yes	Center Scoop	No
Center Scoop & Tooth Complex	ST	Yes	Center Scoop	Yes

The tunnel was seeded using a Corona Vi-Count 5000 thermal smoke generator, which produced 0.2-0.3 μm particles from a mineral oil base. Smoke particles were released into the stagnation chamber of the TWT, to dissipate disturbances introduced by the particle injectors. Particles measured in situ were found to be between 0.7-0.8 μm due to agglomeration, resulting in an estimated Stokes number of 0.02. The light source

was a 400 mJ frequency-doubled dual cavity Spectra Physics PIV-400 Nd:YAG laser, which produced a 1.5 mm thick, 532 nm wavelength laser sheet.

Stereoscopic particle image velocimetry (SPIV) was used to measure the flow field at the center plane of the cavity, as shown in Fig. 2, which also identifies the data coordinate axes. Experiments were conducted according to the setup described by Beresh et al.[11,12] and DeMauro et al.[23] using two commercial LaVision DaVis 8.2 systems, simultaneously. Images were obtained using four LaVision Imager sCMOS cameras with 200 mm lenses and Scheimpflug adapters, each with a resolution of 2560 × 2160 pixels, digitized at 16 bits: two cameras were used to capture the upstream portion of the measurement domain, two the downstream portion. Image pairs were acquired with a time delay between laser pulses of $\delta t = 1.4$ μs.

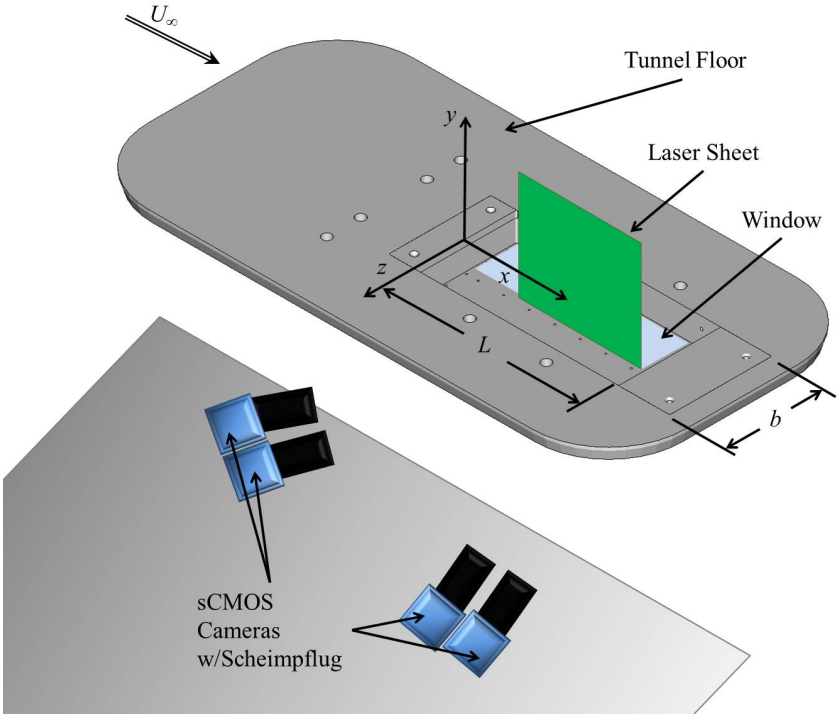

Figure 2. Location of the measurement plane with respect to the SR cavity. The axis origin is located midway on the leading edge of the cavity. The upper surface, indicated by the arrow, identifies the surface of the tunnel floor. Note that D (not shown) is the cavity depth, along the wall-normal (y) direction.

SPIV calibration was performed using a single level 101.6 × 101.6 mm calibration target, which had a square grid of dots spaced 6.35 mm apart. The target was initially positioned at the spanwise centerline of the cavity. The target was mounted on a linear stage that allowed for calibration images to be taken at 7 different spanwise locations (based on the axes in Fig. 2), in increments of 0.25 mm, at $z/D = 0$, ± 0.009, ± 0.017, and ± 0.026.

Within the literature, few studies have been performed that have investigated three-dimensionalities within open cavities experimentally. Crook et al.[15] made measurements in water using multiple 2C PIV planes in various orientations, exploring the flow topology. Likewise, Haigermoser et al. used tomographic PIV to make flow field measurements within deep rectangular[25] and circular cavities,[26] albeit in low-speed flows. In this study, fluid volumes (associated with a transonic flow regime) were measured using a scanning SPIV method. The camera mounting and traverse mechanism are shown in Fig. 3a and b. In order to view into each of the cavities within the constraints of TWT's optical access, a mirror was used to reflect light scattered from the seed particles into the cameras, as seen in Fig. 3c. The cameras were mounted such that each system had a stereo-angle of about 28°, inclusively (half angle of about 14°), with a tilt angle of about 40°. The cameras were mounted on two Newport M-UMR8.51 linear translation stages (51 mm of travel, two cameras per stage), each operated with BM17.51 micrometers (accurate to within 10 μm). Fluid volumes were measured by collecting SPIV measurements at multiple spanwise locations ($z/D = 0$, -0.07, -0.14, -0.21, -0.28, -0.34, -0.41, -0.55, -0.69, -0.83, -0.97, -1.10, -1.17, -1.24, -1.31, -1.38, and -1.45).

SPIV data were processed using a multi-pass method with an initial pass using 64 × 64 pixel interrogation windows, followed by two passes using 32 × 32 pixel interrogation windows, with a 50% overlap. Each

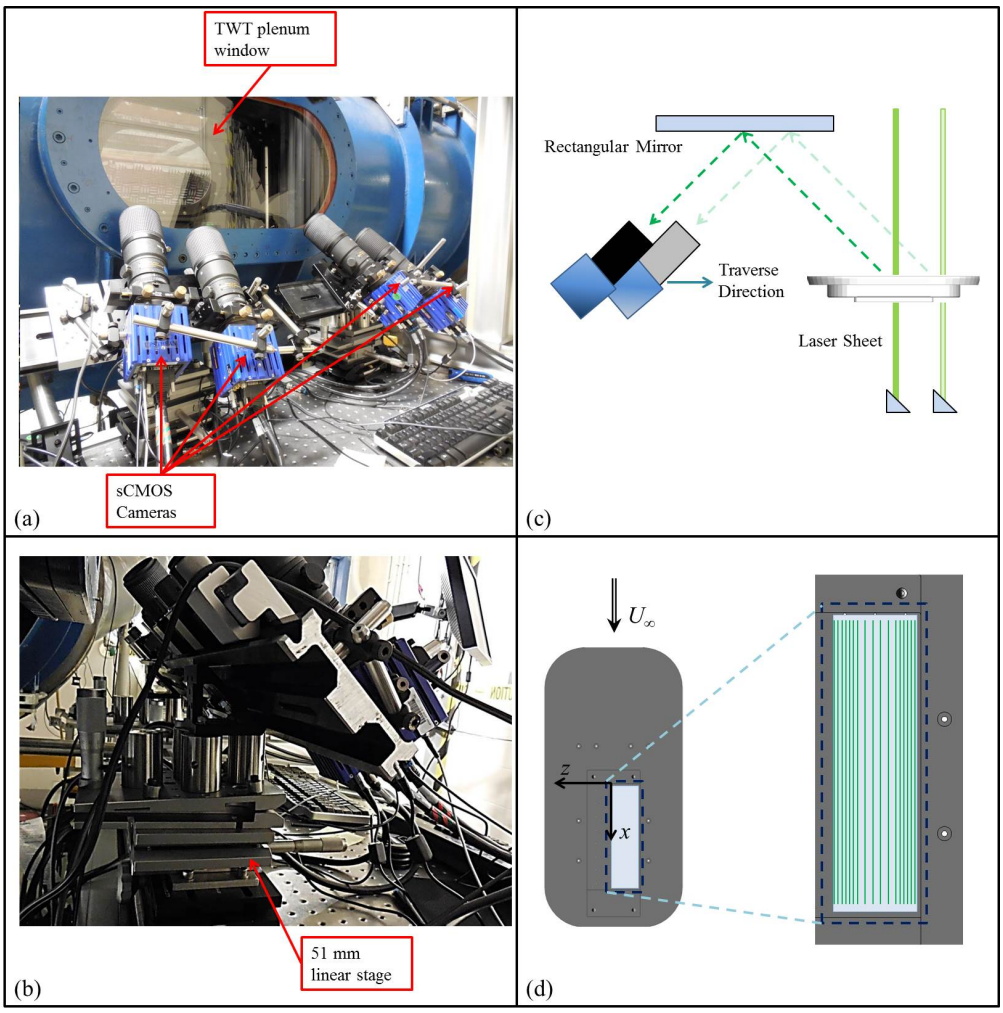

Figure 3. Photographs and schematic of the data collection procedure: (a) cameras mounted at a tilt angle for optical access; (b) mirror used to reflect image into cameras; (c) transparent floor of cavity; (d) schematic of how imaging of the cavity flow field was achieved.

plane represents the average of 900 image pairs, resulting in time-averaged quantities of U, V, and W, along with their associated Reynolds stresses and turbulence intensities. Taking these data, an inverse-distance interpolation was performed in Tecplot, resulting in volumetric measurements of the cavity flows ($2.5 \leq x/D \leq 6.5$, $-0.95 \leq y/D \leq 1.2$, $-1.45 \leq z/D \leq 0$), following the method used by DeMauro et al.[23] Note that the cavity has a width of $b/D = 3.5$; therefore SPIV measurements do not extend out to $z/D = -1.75$ due to limitations on optical access. The planes were interpolated onto a uniform grid in increments of 2 mm in the spanwise direction. The data presented here were smoothed with three passes using the smooth3 algorithm in Matlab. No smoothing was performed on the instantaneous images prior to averaging. An example of the resulting volumetric interpolation can be seen in Fig. 4, which shows the measured planes for the SR cavity and the associated interpolated fluid volume, illustrated using contours of time-averaged total velocity ($V_{tot} = \sqrt{U^2 + V^2 + W^2}$).

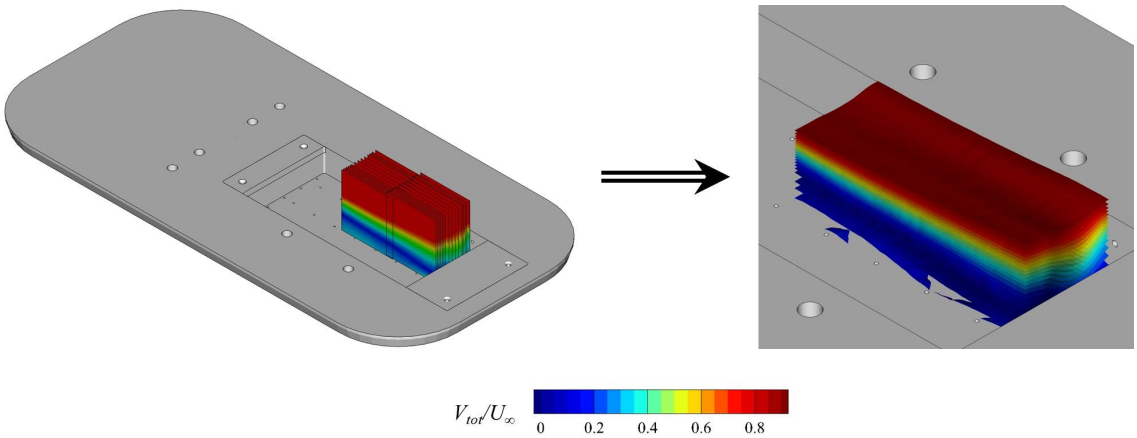

Figure 4. The total collected SPIV planes for the SR cavity and the associated interpolated fluid volume, represented in both instances by contours of V_{tot}.

The precision uncertainty of mean velocity components were determined from $\varepsilon_p = 2\sigma/\sqrt{N}$, where σ is the standard deviation of each velocity component and N is the total number of instantaneous vectors in an average. An estimation of the precision error (across 900 vectors) was obtained from a single downstream spanwise location where local turbulent kinetic energy was observed to be largest, in the SR cavity. Within the shear layer, where standard deviations were seen to be largest, a conservative estimate of the precision errors for U, V, and W were $0.009U_\infty$, $0.008U_\infty$, and $0.009U_\infty$, respectively.

III. Results/Discussion

III.A. Volumetric SPIV Measurement of the Cavities

Inherent in all of the cavity morphologies is a degree of three-dimensionality. This is present even in a rectangular cavity with side edges, which could induce a spanwise effect.[23] This section presents the volumetric data reconstructed from the scanning SPIV measurements in order to provide insight into the physical mechanisms that impact the acoustics of each cavity. The data will be analyzed with respect to U, TKE, vorticity, and Reynolds shear stresses.

III.A.1. Three-dimensional variation of U

Casper et al.[22] showed that the three complex cavities exhibited differences in their modal frequencies and amplitudes, in comparison to the SR case. These differences may be due to the spanwise effects induced by the additional features associated with the complex cavity geometries. The resulting volumes for the four geometries are shown in Fig. 5, illustrated using iso-contours of streamwise velocity. The iso-contours are displayed with 70% transparency in order to better highlight certain features. In addition, iso-contours at $U/U_\infty = 0$, 0.25, and 0.50, are shown with full opacity; specifically, the iso-contour of $U/U_\infty = 0$, which shows the separation between forward and reverse flow within the cavities.

The SR cavity (Fig. 5a) appears relatively two-dimensional closer to the leading edge of the cavity. The mixing layer spreads in the wall-normal direction with increasing distance downstream of the leading

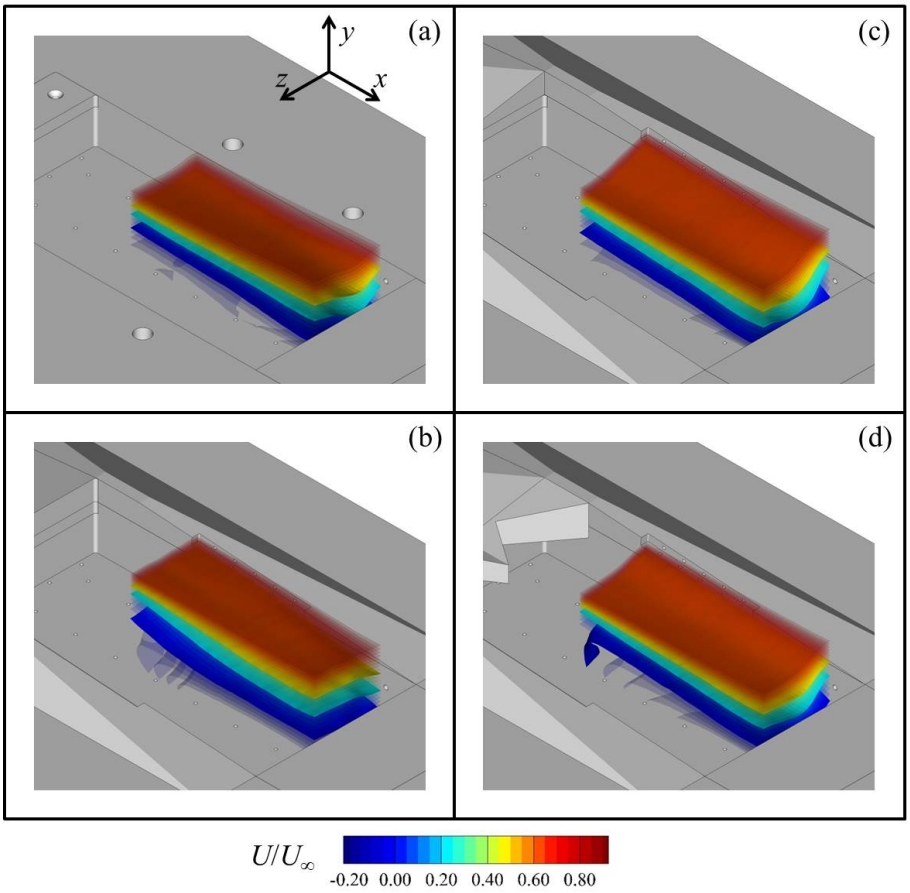

Figure 5. Reconstructed volumes within the four cavity geometries, represented using iso-contours of time-averaged streamwise velocity (U): (a) SR cavity; (b) BC cavity; (c) CS cavity; (d) center scoop & tooth complex cavity. The volumes are shown with 70% transparency, except for iso-contours at levels of $U/U_\infty = 0$, 0.25, and 0.5, which remain opaque. Note that the freestream velocity is parallel to the streamwise direction.

edge, due to growth of the Kelvin-Helmholtz instability (KH) and entrainment of flow by the instability eddies. With increasing distance, a spanwise "waviness" begins to take shape within the mixing layer, being most evident within the $U/U_\infty = 0.25$ and 0.5 iso-contours. Farther downstream, closer to the trailing edge of the SR cavity, this spanwise waviness is more apparent, giving rise to a nearly sinusoidal distribution approximately two wavelengths in size across the span of the cavity. As a consequence of this waviness, a localized region of accelerated flow exists within the SR cavity, nearly halfway between the cavity side edge and centerline.

The BC cavity (Fig. 5b) does not exhibit this type of wavy pattern. The leading edge ramp elevates the mixing layer along the wall normal direction. The combination of the convective acceleration due to the presence of the ramp and the resulting curvature of the mixing layer within the BC cavity has the effect of locally accelerating the time-averaged flow above the cavity by as much as 13% ($M = 0.9$, locally). Nearer to the rear wall, the BC cavity appears to have a thicker mixing layer compared to the SR cavity. By raising the mixing layer vertically, the rear wall of the cavity is impinged upon by a lower momentum portion of the flow. This should result in a reduction of energy transfered into the upstream-propagating pressure waves emanating from this wall, attenuating the resulting Rossiter tones within the BC cavity. In addition, along the spanwise direction, the BC mixing layer turns inward, towards the floor of the cavity, as the side edge is approached.

With the addition of a scooped cut-out in the leading edge ramp, a wavy pattern can be seen once again within the CS cavity (Fig. 5c). This waviness, however, is due to the spanwise angle (5.7°) of the scooped leading edge, which increases from a minimum of $y/D = 0.13$ at centerline to a maximum of $y/D = 0.44$ at the side edge. The addition of the tooth (Fig. 5d) appears to create little difference in this spanwise distribution; however, the iso-contour at $U/U_\infty = 0$ implies that the ST cavity recirculation vortex is centered somewhat farther downstream than in the CS case.

To better appreciate the spanwise dependency of the streamwise velocity, Fig. 6 shows spanwise distributions of U, taken at $x/D = 3.5$, 4.5, and 5.5, and y/D = -0.5, 0, and 0.5, for the four cavities. Note that $y/D = 0$ corresponds to the wall-normal location of the SR leading edge. As mentioned previously, the SR cavity (Fig. 6a) has a relatively two-dimensional spanwise distribution ($x/D = 3.5$, 4.5) that begins to take on a nearly sinusoidal pattern with increasing distance ($x/D = 5.5$). This spanwise wavelength shows an amplitude of nearly $\pm 0.1 U_\infty$ at y/D = -0.5 (∼27 m/s), indicating that this is a non-negligible change in the streamwise velocity. With increasing vertical height, the amplitude of this wavy distribution decreases, until at $y/D = 0.5$, it is barely present in the velocity distribution at all three streamwise locations. This location of the flow field is outside of the cavity mixing layer and within the freestream; therefore increasing height along the wall-normal direction will lead to a more spanwise-uniform flow.

The BC cavity (Fig. 6b) shows more uniformity along the streamwise direction. Unlike the SR cavity, the BC cavity velocity distributions do not appear to gradual change in shape. It can, however, be seen that the velocity distribution begins to approach unity as the side edge of the cavity is approached. It should be pointed out that, as the velocity data does not reach all the way to the side edge of the cavity (at z/D = -1.75), no wall-normal boundary layer is measured here (associated with the no-slip condition along the side wall). In agreement with the volumes shown in Fig. 5c and d, the spanwise distributions for the CS and ST complex cavities are rather similar. Both appear to show a wavy pattern associated with boundary layer separation from a scooped leading edge, however the ST configuration (Fig. 6d) seems to achieve slightly smaller values of U than the CS cavity. In addition, the CS cavity appears to show signs of a spanwise waviness, similar to the SR case (Fig. 6c, at y/D = -0.5).

The data shown thus far has indicated the existance of a large degree of three-dimensionality that exists within the cavity flow fields. In regards to the spanwise waviness evident in the SR cavity, a question that arises is whether or not this waviness is evidence of a spanwise instability.[6,7,9] The spanwise instability is a centrifugal instability that is associated with the recirculation vortex.[6] It was shown within the work of Brès & Colonius that the instability was identifiable from a BiGlobal linear stability analysis of a two-dimensional base flow. This analysis assumes that no spanwise dependency exists for any of the three (time-averaged) velocity components; therefore this base flow is not representative of the time-averaged velocity fields shown here. In contrast, the waviness shown here (as will be discussed later) is due to the presence of developing vortices (in the time-average) associated with separation of a spanwise boundary layer along the side edges of the cavity. This is not an instability in the classical sense; rather a developing feature of the base flow. The interaction between these two mechanisms (streamwise vorticity and spanwise instability), however, remains unclear at this time and warrants further investigation.

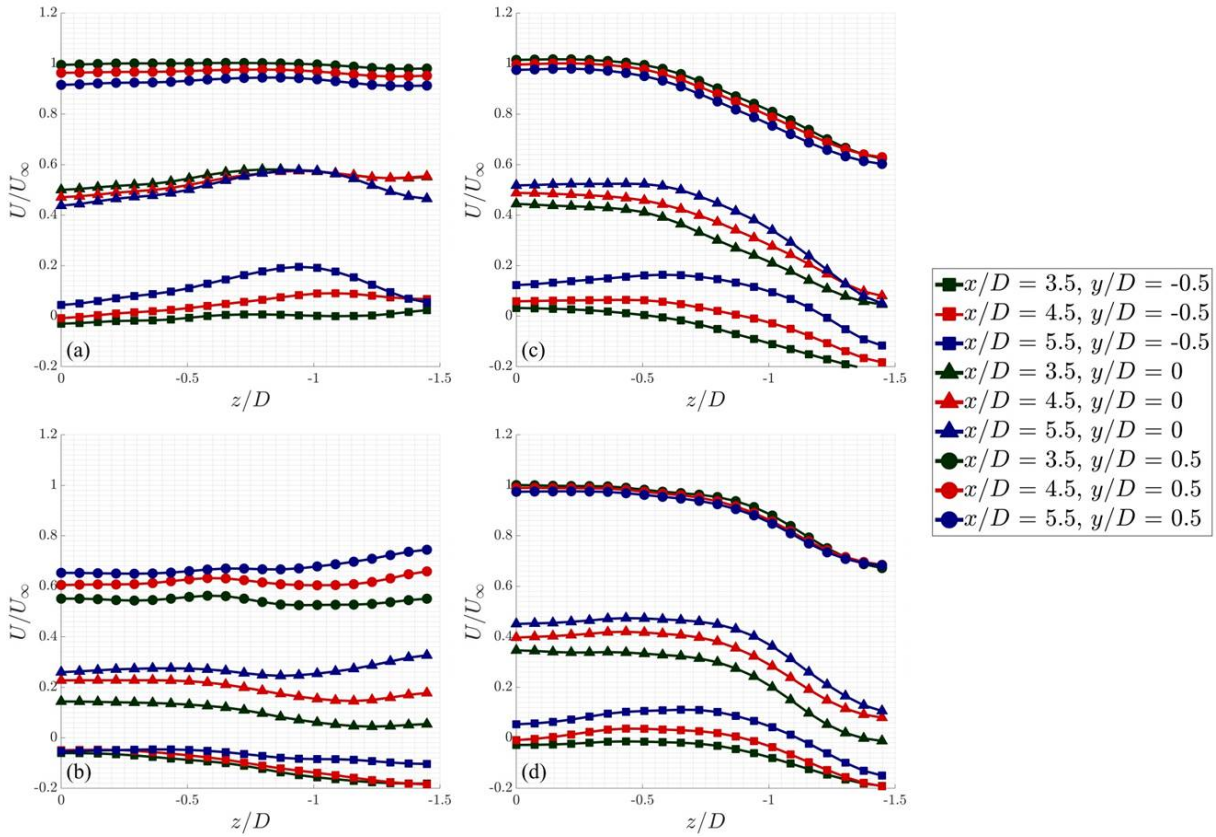

Figure 6. Spanwise distributions of U at various streamwise and wall-normal locations for the: (a) SR cavity; (b) BC cavity; (c) CS cavity; (d) ST cavity.

III.A.2. Three-dimensional variation of TKE

The localized increase in streamwise velocity within the SR cavity must be attributable to momentum transfer, and therefore increased mixing from the freestream inward towards the floor of the cavity. To better illustrate this fact, iso-contours of TKE are shown in Fig. 7 for the corresponding cavities seen in Fig. 5, where TKE is defined as $\frac{1}{2}\overline{u_i' u_i'}$, with u_i' being the fluctuating component of velocity obtained from Reynolds decomposition of the velocity field: i.e., $u_i(x_i,t) = U_i(x_i) + u_i'(x_i,t)$. Therefore, the TKE (and later, the Reynolds shear stresses) shown here contain contributions from both random and coherent motions. Here, the iso-contours are displayed with 80% transparency in order to better highlight certain features. In addition, the iso-contour corresponding to TKE = 0.06 is shown with full opacity.

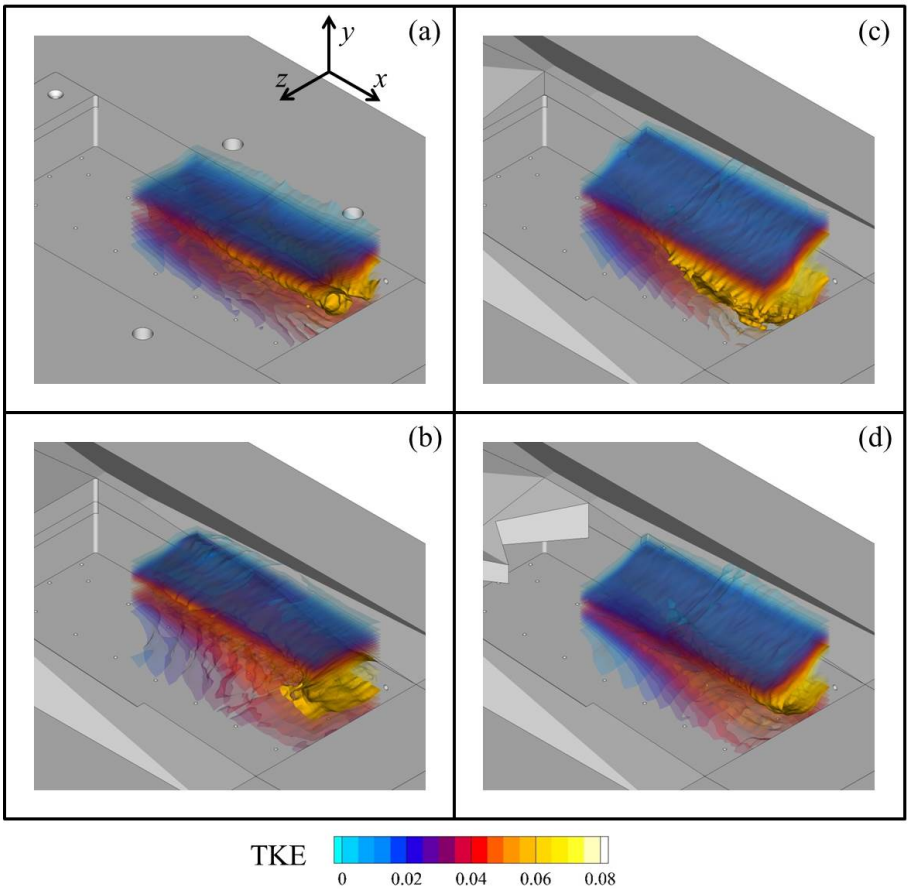

Figure 7. Reconstructed volumes within the four cavity geometries, represented using iso-contours of turbulent kinetic energy (TKE): (a) SR cavity; (b) BC cavity; (c) CS cavity; (d) ST cavity. The volumes are shown with 80% transparency, except for an iso-contours at levels of TKE = 0.06, which remains opaque. Note that the freestream velocity is parallel to the streamwise direction.

In all cases, the magnitude of the TKE increases with increasing streamwise distance. As the rear wall of the cavity is approached, impingement of the mixing layer on this surface results in larger TKE at the rear of the cavity. In addition, as the flow direction reverses at the rear corner, a region of higher TKE can be seen to extend nearly to the floor of the cavity. Within the SR cavity, a pair of longitudinal structures appear in the center of the mixing layer (opaque structures in Fig. 7a). These regions of high TKE represent locations of increased turbulent mixing within the mixing layer. As was seen in DeMauro et al.[23] and will be shown in later sections, these correspond to the locations of maximum influence by streamwise vortical structures within the cavity.

In contrast, the BC cavity (Fig. 7b) does not appear to have these longitudinal structures; the largest magnitudes of TKE in this case are associated almost entirely with the rear wall impingement. Compared to the SR cavity, there appears to be a much greater degree of TKE spread throughout the cavity, which may be associated with turning of the mixing layer at the rear corner. Furthermore, the BC cavity appears to have a much thicker mixing layer than the SR cavity.

The CS cavity (Fig. 7c) mixing layer lifts away from the floor of the cavity as the side edge is approached, due to the angle associated with the center scoop. A portion of the mixing layer, however, appear to remain parallel to the trailing edge of the cavity, near the centerline. In comparison to the BC, the CS cavity shows larger values of TKE across a greater region. With the addition of the tooth (Fig. 7d), the mixing layer appears to thin to a degree. In addition, the presence of the tooth seems to reduce levels of TKE within the cavity, compared to those found in the CS case. This is evident especially from the iso-contour level of 0.06, whick encompasses a large region within the CS cavity, whereas in the ST cavity, this iso-contour is concentrated strictly in the rear corner of the cavity.

III.A.3. Planar slices of TKE

Although not as readily evident from Fig. 7, a spanwise dependency exists for TKE within each of the cavities. To further highlight this, Fig. 8 shows color contours of TKE with in-plane streamlines, for the four cavities at $z/D = 0$, -0.72, and -1.23. Larger regions of TKE are primarily associated with the mixing layer, which again can be seen to widen in all cases with increasing streamwise distance. As was previously mentioned, due to the redirection of flow upon impingement on the rear wall of the cavity, a region of TKE exists nearer to the floor of the cavities.

At $z/D = 0$, the SR cavity (Fig. 8a) shows the presence of two co-rotating recirculation vortices: a main vortex at $x/D \approx 3$, and a secondary rear vortex at $x/D \approx 6$. The existence of this rear vortex was attributed by Crook et al. to being a function of Reynolds number and thickness of the on-coming boundary layer just prior to separation at the leading edge.[15] However, no similar structure was shown within the work of Beresh et al.[12,27] or Wagner et al.,[28] which were conducted in similar conditions, albeit for a smaller length cavity. As noted by Beresh et al.,[27] Rossiter mode 1 appears to behave like a standing wave whose wavelength may exceed the length of their cavity ($L = 127$ mm). The longer cavity length seen in this study ($L = 203.2$ mm) may allow for portions of the standing wave to appear that manifest in the time-averaged velocity field as the presence of this rear vortex. In addition, comparison to the TKE measurements of Beresh et al.[12] show that this cavity exhibits slightly larger values of TKE. This may also be associated with the larger length ($L/D = 7$) compared to that of Beresh et al. ($L/D = 5$), along with the presence of the rear vortex.

Moving off centerline, at z/D = -0.72 (Fig. 8b), the rear vortex is suppressed. An increase in TKE is apparent at this location, along with increased flow being directed towards the floor of the cavity at $x/D > 4$, indicating an acceleration of the wall-normal velocity component. This redirected wall-normal velocity entrains high-speed flow into the cavity, providing an attenuation of reverse flow and implying a degree of pressure recovery. In addition, the size of the primary recirculation vortex has increased along the streamwise direction, extending to $x/D > 6$. Closer to the side edge of the cavity (z/D = -1.23, Fig. 8c), the rear vortex reappears, albeit shifted slightly downstream. This comes with an increase in TKE across much of the plane. This increase in TKE with increasing distance from the centerline shows agreement with Arunajatesan et al.,[14] who saw a similar trend within their $L/b = 1.67$ case (aspect ratio of 0.6).

The BC cavity (Fig. 8d-f) shows larger levels of TKE than the SR cavity. Prior to separation at the leading edge of the cavity, the oncoming boundary layer is accelerated by the favorable pressure gradient that exists on the leading edge ramp, creating a larger $\partial U/\partial y$ velocity gradient. Initially the mixing layer of the BC cavity appears to be thinner than the SR cavity, for $x/D \lesssim 3$; at $x/D > 3$, it appears to become thicker than the SR cavity. A single, large recirculation vortex is apparent at $x/D \approx 4$, which shifts slightly downstream closer to the side wall of the cavity (Fig. 8f). Likewise, as the mixing layer issues from a higher vertical point than in the SR case, the length scale of the recirculation vortex is increased. As the side edge of the cavity is approached, the levels of TKE within the mixing layer appear to gradually increase, however the location of maximum TKE within the mixing layer shifts upstream. At centerline (Fig. 8d), TKE is maximum near the rear wall; at z/D = -0.72 (Fig. 8e), TKE is nearly evenly distributed; finally, at z/D = -1.23 (Fig. 8f), its focus is oriented at $x/D \approx 3.5$. Furthermore, the rear of the BC cavity shows larger wall-normal velocity directed towards the floor of the cavity. Referring to the mixing layer, the rear wall of the BC cavity sees a reduced level of streamwise momentum impinge upon it. The reduced streamwise impingement, increased wall-normal velocity, and increased TKE may all result in a weakening and dissipation of Rossiter modal structures.

By decreasing the leading edge at centerline(Fig. 8g-i), the CS cavity shows an increase in TKE compared to the BC cavity. Across all three spanwise locations, the CS cavity seems to have a thicker mixing layer than either the SR or BC cavities. The recirculation vortex at centerline (Fig. 8g) is more similar to the SR cavity, with a center located at $x/D \approx 3$. In addition, there appears to be evidence of a weak rear

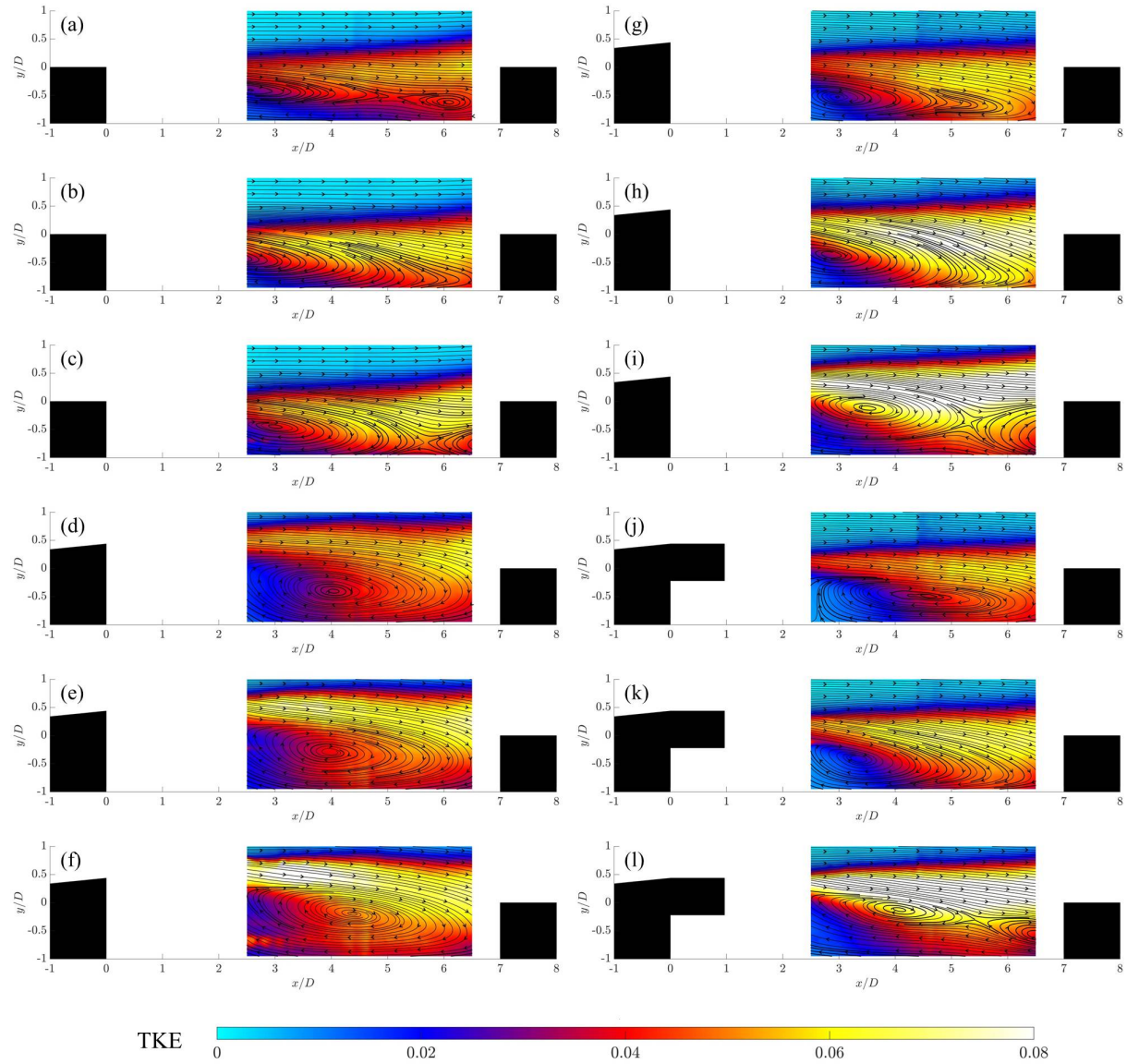

Figure 8. Color contours of TKE superimposed with in-plane streamlines in the xy-plane for the SR cavity: (a) z/D = 0, (b) z/D = -0.72, (c) z/D = -1.23; BC cavity: (d) z/D = 0, (e) z/D = -0.72, (f) z/D = -1.23; CS cavity: (g) z/D = 0, (h) z/D = -0.72, (i) z/D = -1.23; ST cavity: (j) z/D = 0, (k) z/D = -0.72, (l) z/D = -1.23. Note that the black silhouettes represent the cavity edges.

vortex at $x/D \approx 5$. By reducing the height of the leading edge at centerline, the CS cavity initially has a thicker mixing layer than the BC cavity; the flow is locally accelerated to a much smaller degree prior to separation at the leading edge. At $x/D \lesssim 3$, the CS mixing layer shows levels of TKE comparable to the SR cavity; beyond this, TKE rapidly increases as the rear wall is approached. At z/D = -0.72 (Fig. 8h), a large scale increase of TKE is evident, along with a lengthening of the recirculation vortex along the streamwise direction, similar to the SR cavity at the same spanwise location (Fig. 8b). At z/D = -1.23 (Fig. 8i), the recirculation vortex shifts somewhat downstream, and a rear vortex becomes evident. Similarly to the SR and BC cavities, the three planes show that the mixing layer TKE increases in magnitude with increasing distance from the centerline, while the upper surface of the mixing layer rises.

Figure 5 showed little apparent difference between the CS and ST cases, other than an apparent movement of the recirculation vortex along the streamwise direction. However, this appears not to be the case with regards to the TKE and cavity recirculation, as shown in Fig. 8j-l. With the addition of the tooth, the centerline mixing layer appears to have thinned, with slight decreases in the magnitude of TKE (Fig. 8j). Interestingly, the recirculation within the ST configuration appears to be more similar to the BC cavity (Fig. 8d), with a single recirculation vortex centered at $x/D \approx 4.5$. Moving off centerline to z/D = -0.72 (Fig. 8k), the ST cavity begins to resemble the CS configuration (Fig. 8h) with the appearance of an elongated recirculation vortex, albeit with a thinner mixing layer and lower values of TKE. The core of the recirculation vortex has shifted upstream to $x/D \approx 3.3$. At z/D = -1.23 (Fig. 8l), the ST cavity appears nearly indistinguishable from the CS cavity (Fig. 8i), except for the slightly thinner mixing layer. It can also be seen here that the core of the recirculation vortex has moved downstream to $x/D \approx 4$. As the upward displacement of the mixing layer seen in Fig. 5c and d and Fig. 7c and d is associated with the presence of the scoop, the streamwise movement of the ST recirculation vortex is associated with the jagged morphology of the tooth (Fig. 1d); in locations where the leading edge is protruding into the cavity, the vortex moves downstream, whereas it moves upstream where the leading edge does not protrude.

In addition to spanwise slices, streamwise planes are shown in Fig. 9 for the same four cavities, at x/D = 3, 4, and 5. As was previously mentioned, the mixing layer of the SR cavity (Fig. 9a-c) has a gradually increasing level of TKE with increasing streamwise distance. In all three planes, the two regions of high TKE identified in Fig. 7a are evident, at $z/D \approx$ -0.5 and -1.4. These regions increase in magnitude with increasing distance downstream; with an effect reaching nearly to the floor of the cavity at x/D = 4 and 5 (Fig. 9b and c, respectively). Again, as the rear wall is approached, TKE increases within the cavity (y/D < 0), in order to encompass the unsteadiness associated with the flow impinging on the rear wall. The origin of the two regions of large TKE will be discussed in the subsequent sections.

Due to the presence of the larger recirculation vortex within the BC cavity, evidence of high TKE associated with mixing layer impingement and redirection can be seen closer to the leading edge than in comparison to the SR cavity. At x/D = 3 (Fig. 9d), the mixing layer is clearly thinner than the mixing layer of the SR cavity at the same streamwise location. Moving downstream to x/D = 4 (Fig. 9e), the mixing layer has increased in thickness; although elevated in the vertical direction, its influence reaches nearly to the cavity floor. Farther downstream (x/D = 5, Fig. 9f), there is a clear global increase in TKE within the cavity, as the rear wall is approached. In addition, a region of increased TKE is identifiable at $z/D \approx$ -1; this most likely corresponds to the point of entrainment of side-wash spillage into the mixing layer. As was seen in Fig. 8d-e, the location of maximum TKE appears to be centered at $x/D \approx 3.5$, which is equivalent to the mid-length of the cavity. Evidence of this maximum can be seen in Fig. 9e, which corresponds to x/D = 3. This point will be addressed in the subsequent sections.

In contrast to the SR and BC cavities, the CS cavity (Fig. 9g-i) has shown that the influence of the 5.7° spanwise angle to the leading edge cut-out continues to be felt across the streamwise length of the cavity. At x/D = 3 (Fig. 9g), it can be seen that the CS cavity mixing layer (at centerline) is situated at a lower vertical height, compared to the BC cavity. The upwards inclination of the mixing layer does not appear to being until $z/D \approx$ -0.5. Moving towards the side wall of the cavity, there is a noticeable increase in TKE, along with a constant angling upwards of the mixing layer. At x/D = 4 (Fig. 9h), the level of TKE throughout much of the cavity has greatly increased; a trend that continues downstream to x/D = 5 (Fig. 9i). The high levels of TKE indicate a large degree of turbulent mixing occurs within this cavity.

The ST cavity (Fig. 9j-k), again behaves similar to the CS configuration, with a few notable differences. The mixing layer is noticeably thinner at all locations, and there are reduced levels of TKE across much of the cavity. Futhermore, the region of high TKE near the side edge of the cavity appears to be smaller and more localized. Figure 9j shows that, at x/D = 3, the mixing layer appears to have a relatively constant

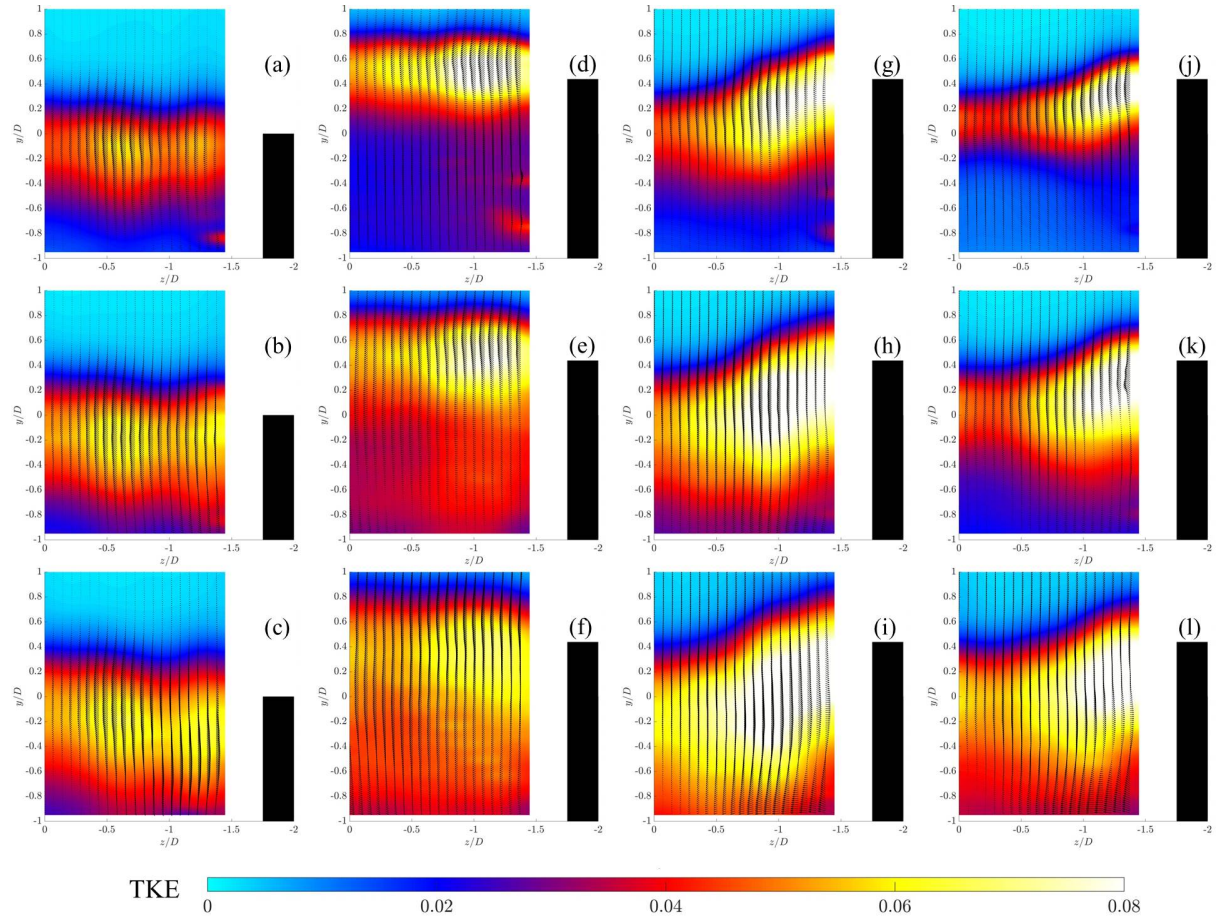

Figure 9. Color contours of TKE with superimposed in-plane velocity vectors in the yz-plane for the SR cavity: (a) $x/D = 3.0$, (b) $x/D = 4.0$, (c) $x/D = 5.0$; BC cavity: (d) $x/D = 3.0$, (e) $x/D = 4.0$, (f) $x/D = 5.0$; CS cavity: (g) $x/D = 3.0$, (h) $x/D = 4.0$, (i) $x/D = 5.0$; ST cavity: (j) $x/D = 3.0$, (k) $x/D = 4.0$, (l) $x/D = 5.0$. Note that the black silhouettes represent the cavity edges.

elevation above the floor of the cavity, extending from centerline to $z/D \approx$ -0.5. Within this region, the reduced levels of TKE compared to the CS cavity might lead to a reduced rate of dissipation of structures within the mixing layer. At $x/D = 4$ and 5 (Fig. 9k and l), a secondary (albeit weaker) concentration of TKE can be seen just off centerline. This may signify increased mixing associated with streamwise vorticity issuing from the protruding cavity tooth. In order to investigate this further, it is necessary to examine the streamwise vorticity within each of the cavities.

III.A.4. Three-dimensional variation of ω_x

To demonstrate the presence of streamwise vorticity within the cavities, iso-contours of time-averaged ω_x are shown in Fig. 10 for all four cavities, with ω_x defined as $\partial W/\partial y - \partial V/\partial z$. The iso-contours are presented with 80% transparency except for a single contour corresponding to $\omega_x D/U_\infty =$ -0.1. Because of the presence of discontinuities in the wall-normal and spanwise velocity components associated with the large camera tilt angle, these contours were smoothed six times. Even so, these contours illustrate not only the presence but relative location and shape of structures within the cavities.

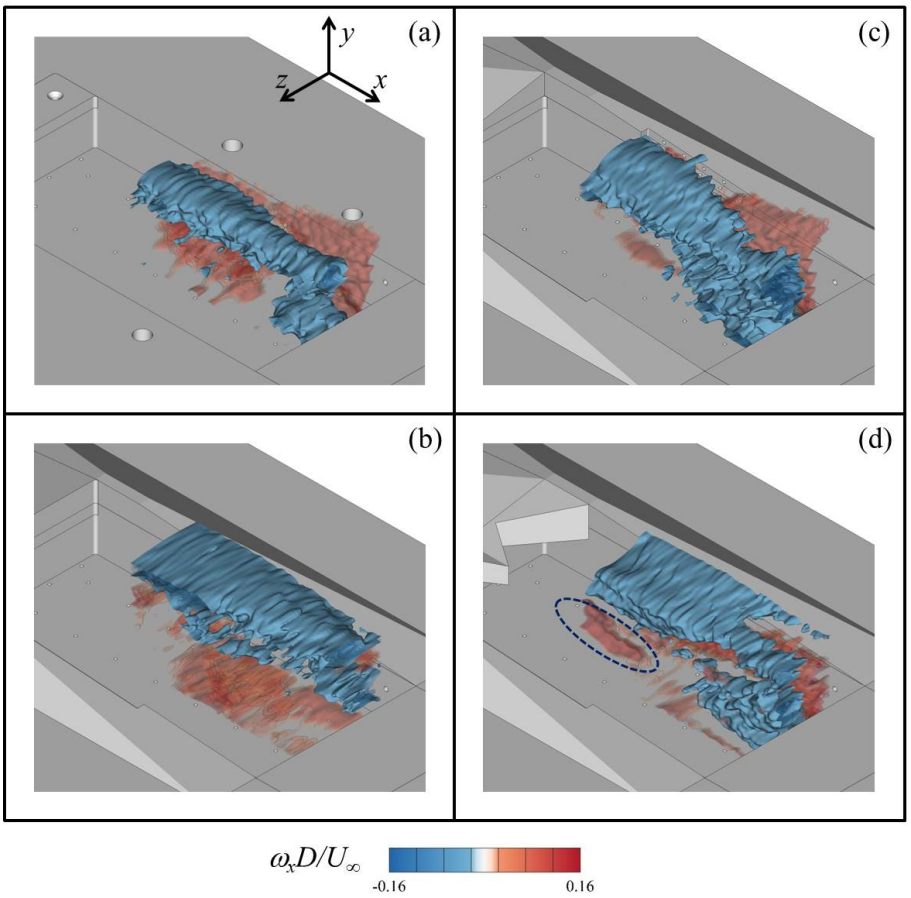

Figure 10. Reconstructed volumes within the four cavity geometries, represented using iso-contours of time-averaged streamwise vorticity (ω_x): (a) SR cavity; (b) BC cavity; (c) scoop complex cavity; (d) ST cavity. The volumes are shown with 80% transparency, except for an iso-contours at levels of $\omega_x D/U_\infty$ = -0.1, which remains opaque. Note that the freestream velocity is parallel to the streamwise direction.

The SR cavity (Fig. 10a) contains a counter-rotating vortex pair: a structure with a positive sense near to the wall, and a secondary structure with a negative sense closer to the centerline of the cavity. This secondary structure sits above the mixing layer height, offset vertically from the spillage vortex.[23] Flow is drawn into the cavity along the leading edge and side edges due to a low pressure region within the cavity. As the flow enters along the side edge, this side-wash spillage separates at that edge, resulting in the formation of a streamwise vortex that grows with increasing streamwise distance due to flow entrainment. Furthermore, this spillage vortex induces a secondary, counter-rotating vortical structure closer to the centerline of the cavity, situated above the mixing layer. The presence of this induced counter-rotating vortex appears to

be a function of the width of the cavity: if the cavity is too narrow, then only the spillage vortices are present; if the cavity is wide enough, these induced secondary structures are present.[13] The combination of the counter-rotating vortex pair creates an induced velocity in towards the floor of the cavity, increasing momentum transfer into the cavity and locally increasing cavity velocity.

The BC cavity (Fig. 10b) has a different vortical pattern. The leading edge ramp and the side ramps of the BC cavity create a favorable pressure gradient that locally accelerates the flow prior to separation at the leading edge and side edges. Recall that the side ramps have angles of 26.6°, compared to the leading edge ramp angle of 5.7°, resulting in greater convective acceleration. Furthermore, the local acceleration of the flow also reduces the local pressure, decreasing the tendency for the side-wash spillage to enter into the cavity. Instead, this spillage is entrained into the mixing layer issuing from the leading edge, giving rise to the curvature of the BC cavity mixing layer and to the presence of only a single large region of vorticity about the mixing layer.[23] This interaction between the side-wash spillage and the mixing layer gives rise to the region of large TKE seen in Fig. 9d-f. As was seen in Fig. 8f, a region of large TKE is concentrated around $x/D \approx 3.5$, i.e. mid-length. The reason for this will be elaborated on in the following section.

The CS cavity (Fig. 10c) sees a return of a counter-rotating vortex pair similar to that seen in the SR cavity. The presence of scoop provides for the formation of streamwise vorticity to begin from the apex of the cut-out, traveling along the edges of the cut-out and continuing along the cavity side edges. This again induces the formation of a secondary, counter-rotating structure closer to the centerline of the cavity. Due to the presence of the side ramps like the BC case, the CS cavity most likely also sees entrainment of side wash like the BC cavity. This would result in the broad appearance of the induced vortex in this case. Looking back at Fig. 6c, at y/D = -0.5 (where the effect of these vortices was the strongest in the SR case), a small scale sinusoidal waviness can once again be seen to take shape in the CS cavity, due to the influence of these vortices, according to the same mechanisms described for the SR cavity. Note that this effect is reduced, due to the spanwise variation in mixing layer height from the floor of the cavity.

The ST configuration (Fig. 10d) also displays a spillage vortex structure, although much weaker in comparison to the CS cavity. The presence of the jagged leading edge appears to interfere with the formation of the spillage vortex. As there is likely still entrainment of side wash in the ST cavity in a manner similar to the BC cavity, this results in a large region of negative vorticity similar to the BC cavity. It should be noted that although the apex of the tooth is symmetric about the centerline of the cavity, the jagged pattern is not. For this reason, a single vortical structure with positive vorticity (identified by the dotted-line circle in Fig. 10d) is identifiable along centerline. This structure, while strong in magnitude, appears to dissipate rapidly downstream, as at these contour levels, it does not extend along the entire length of the cavity. Referring to Fig. 9j-l, the presence of this vortex can be seen within the small region of TKE located at $y/D \approx 0$, z/D > -0.25.

III.A.5. Cavity Reynolds shear stresses

The presence of streamwise vorticity gives rise to the three-dimensionalities present within the cavities. However, the link between the larger regions of TKE within the mixing layer and the presence of (or lack thereof) spillage vortices is not readily apparent. This section seeks to unify these two points by recourse to the Reynolds shear stresses within the cavities. Figure 11 shows contours of the three components of Reynolds shear stress ($\overline{u'v'}$, $\overline{u'w'}$, and $\overline{v'w'}$), taken at the wall-normal location of the leading edge lip for each of the four configurations. As with the TKE, the Reynolds shear stresses are determined from a Reynolds decomposition of the velocity field. In each figure, in-plane streamlines are included in order to highlight the redirection of side wash spillage along the length of the cavity.

Each of the cavities shows a large degree of interaction between the streamwise and wall-normal velocity components, as a non-negligible level of $\overline{u'v'}$ can be seen across a large area (Fig. 11a, d, g, and j). This shear stress would be associated with eddy convection downstream within the mixing layer, along with Rossiter modal structures. Because a triple-decomposition of the velocity field was not performed, the presence of these coherent structures manifest as large quantities of $\overline{u'v'}$, compared to the other shear stress components. In contrast, levels of $\overline{u'w'}$ are much smaller (except near locations of the streamwise vortices mentioned previously), compared to the other two shear stress components. This may be related to the difference of an order of magnitude between the streamwise and spanwise velocity components. Finally, a large level of $\overline{v'w'}$ was measured in all cavities: in the SR cavity case, they are limited to longitudinal streaks (Fig. 11c); in the BC cavity, a large region issues from mid-length of the cavity, hugging the cavity side wall (Fig. 11f); in the two scoop configurations (Fig. 11i and l), large regions also hug the side wall, but are less

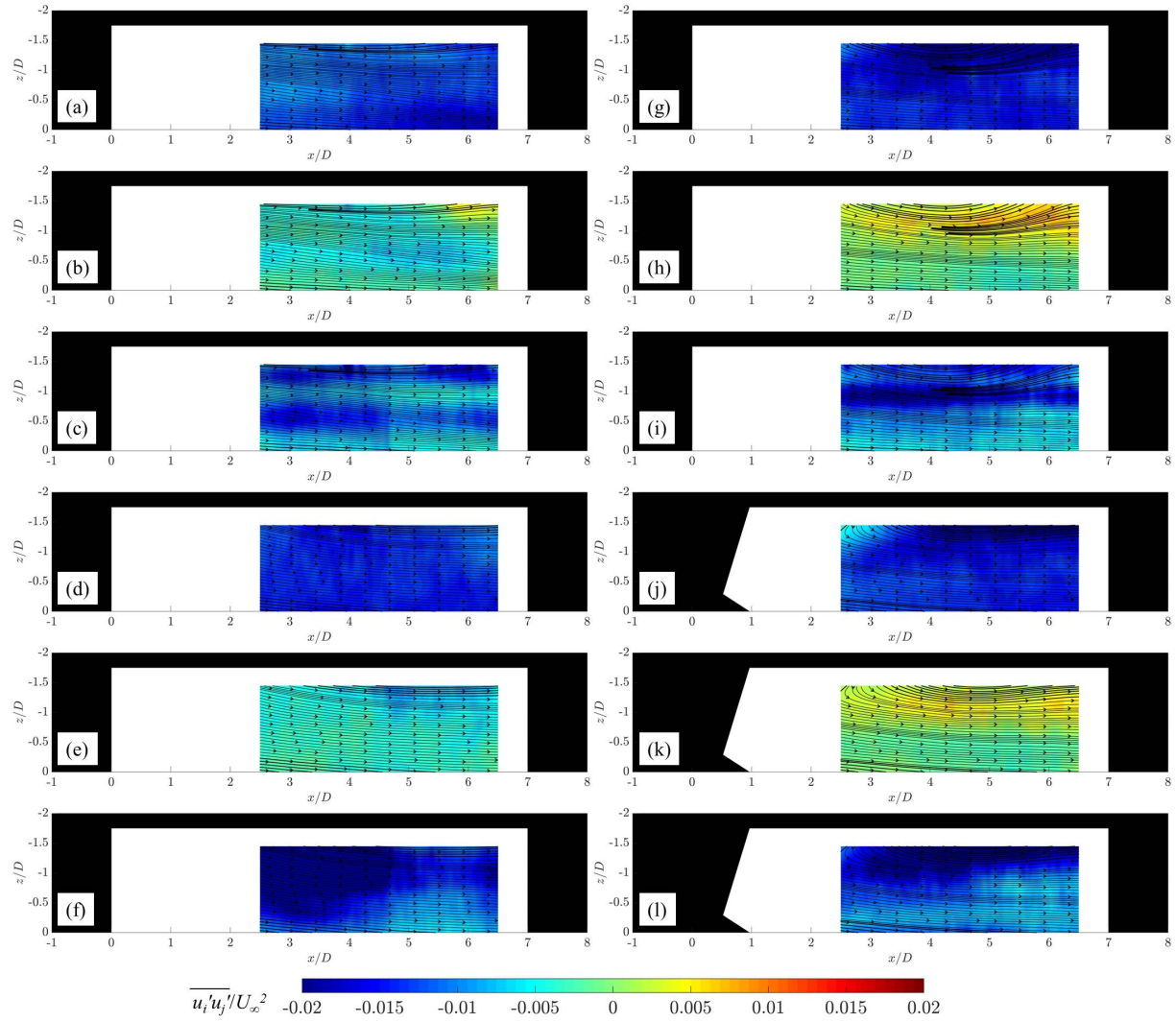

Figure 11. Color contours of Reynolds shear stresses superimposed with in-plane streamlines, taken at the leading edge height at centerline for the four cavities : SR cavity (a) $\overline{u'v'}$, (b) $\overline{u'w'}$, (c) $\overline{v'w'}$; BC cavity (d) $\overline{u'v'}$, (e) $\overline{u'w'}$, (f) $\overline{v'w'}$; CS cavity (g) $\overline{u'v'}$, (h) $\overline{u'w'}$, (i) $\overline{v'w'}$; ST cavity (j) $\overline{u'v'}$, (k) $\overline{u'w'}$, (l) $\overline{v'w'}$. Note that the black silhouettes represent the cavity edges.

localized compared to the BC cavity.

Entrainment of the side wash spillage within the SR cavity appears to be governed by the presence of the spillage vortex (Fig. 11a-c). As was mentioned previously and shown in Fig. 10a, the spillage and secondary induced vortices within the SR cavity are offset in height, with the spillage vortex residing inside the cavity and the secondary induced vortex lying above the mixing layer.[13,23] As a result, both vortices can induce a net spanwise velocity moving inwards towards the centerline of the cavity, resulting in two streaks of $\overline{v'w'}$ with the same directionality (Fig. 11c). Although to a much lesser extent, these vortices also cause a degree of interaction between the spanwise and streamwise velocity components(Fig. 11b). A longitudinal streak at $z/D \approx$ -0.5, indicates the location where this interaction results in the localized acceleration of the streamwise velocity within the cavity (Fig. 5a). It can be seen that these streaks are representative of the interaction of the streamwise vortices (Fig. 10a) with the streamwise velocity component.

The BC cavity shows that the accelerated spanwise velocity leaving the side ramp interacts with the wall-normal velocity component at $x/D \approx 3.5$ (Fig. 11f), which is the location of maximum height of the side ramp (Fig. 1b). Downstream of this location, the side ramp is angled downwards towards the floor of the tunnel, reducing this effect. As is seen in Fig. 8d-f, the large $\overline{v'w'}$ shear stress results in flow being directed downwards towards the floor of the cavity, which also enlarges the BC cavity's recirculation vortex. This mechanism gives rise to the large region of negative vorticity seen in Fig. 10b, where the $\partial V/\partial z$ vorticity component dominates over $\partial W/\partial y$ (i.e., the BC cavity has increasing values of negative V as the side wall is approached). Compared to the SR cavity, there is nearly no $\overline{u'w'}$ shear stress present in the BC (at this wall-normal location), except for a small amount near the rear corner (Fig. 11e).

The two scooped configurations show a degree of commonality in regards to their trends. In both instances, spanwise velocities are much larger (as seen from the streamlines) compared to the SR and the BC cavities, along the side wall. Both of these cavities show increased $\overline{u'w'}$ along the side edge of the cavity (Fig. 11h and k). As was shown in Fig. 5c and d, the mixing layers of these two cavities move away from the floor of the cavity at a function of spanwise distance from the centerline; therefore these increases may be associated with the fact that the mixing layer is at an angle to the xz-plane near the side wall of the cavity. Similar trends are also seen within the associated $\overline{v'w'}$ components seen in Fig. 11j and l.

Comparing the SR and BC cavities to the two scooped complex cavities, the identified trends appear to be associated with the ramp geometries (at the wall-normal locations corresponding to the centerline leading edge). In Fig. 11g-l, the presence of the scooped cut-out appears to be a greater factor to the Reynolds stress distributions than the presence of the tooth. Likewise, the side ramp in the BC cavity results in large increases in $\overline{v'w'}$ compared to the SR cavity.

III.B. Impact of Flow Physics on Cavity Acoustics

As previously mentioned, the results obtained by Casper et al.[22] indicate that changes to the power spectra within the cavities are achievable through manipulation of the cavity morphology. This is evident from Fig. 12, which shows power spectral density (PSD) measurements for the four cavity morphologies, at forward and aft locations along centerline.

Readily apparent from Fig. 12 is the fact that the aft PSD measurements demonstrate stronger magnitudes than the forward measurements. Estimation of the frequencies (but not the amplitudes) of the Rossiter tones (f_m) within an open cavity can be made using the semi-empirical modified Rossiter equation:[29,30]

$$f_m = \frac{m - \alpha}{\frac{1}{\kappa} + M_\infty \left(1 + \frac{1-\gamma}{2} M_\infty^2\right)^{-\frac{1}{2}}} \frac{U_\infty}{L} \tag{1}$$

where $\kappa = 0.57$ is an estimate of the convective velocity of the coherent structures associated with the Rossiter tones within the cavity, $\alpha = 0.25$ is the phase lag between the KH instability and the generated pressure wave, and m is the Rossiter mode. Estimates for the first five modal frequencies and their associated Strouhal numbers (St_m), corresponding to the SR cavity, are shown in Table 2. Comparison between the values shown in Table 2 and the PSD of Fig. 12 show that the dominant frequencies in the SR cavity correspond well with the Rossiter modal frequency estimates obtained from Eq. (1). The volumetric SPIV data presented in the current study may help to explain some of the features that are apparent in Fig. 12.

A purely two-dimensional rectangular cavity would have a mixing layer independent of influence from side-wash spillage. As a result, the TKE and Reynolds stresses associated with a 2D cavity would be due solely to the mixing layer instabilities. With the addition of spillage associated with three-dimensionality,

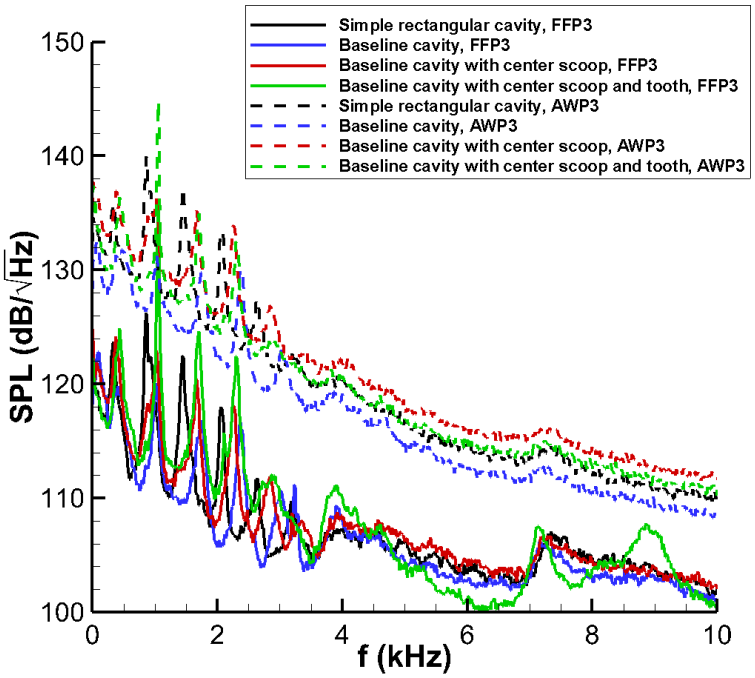

Figure 12. PSD showing sound pressure level vs. frequency for the four complex cavity configurations shown in Fig. 1. FFP3 is the centerline forward floor pressure tap located at x/D = 0.07, y/D = -1.00; AWP3 is the centerline rear wall tap at x/D = 7.00, y/D = -0.57. Taken from Casper et al.[22]

Table 2. Estimations of Modal Frequencies in the Rectangular Cavity (M_∞ = 0.8)

m	St_m	f_m (Hz)
1	0.299	400
2	0.698	930
3	1.097	1460
4	1.495	1990
5	1.894	2520

it has been shown that Reynolds shear stresses associated with the spanwise velocity component are non-negligible and interact with the mixing layer. This could act to rob energy from the KH instability within the mixing layer and reduce the strength of the Rossiter modes in comparison to a 2D cavity; in fact, evidence of this has already been shown by Ahuja & Mendoza, who did report an attenuation of the Rossiter amplitudes with a narrowing of the rectangular cavity.[2]

The BC cavity consistently demonstrates reduced amplitudes for the Rossiter modes, along with a shift in the modal frequencies. The BC cavity differed from the SR cavity by the presence of a larger, single recirculation vortex, along with increased TKE and an apparent lack of a spillage vortex. Due to the presence of the leading edge ramp, the leading edge of this cavity is elevated along the wall-normal direction above the trailing edge of the rear wall. The presence of this ramp resulted in a strengthening of the mixing layer and an increase in mixing layer TKE As the mixing layer impinges on the rear wall and flow is redirected back upstream, the BC cavity shows greater levels of TKE than seen in the SR cavity, which may have the effect of weakening the upstream-propagating pressure waves. Although spillage vortices were not present, the data show that side-wash spillage does in fact interact with the mixing layer, imparting momentum to the wall-normal velocity component. In addition, high levels of mixing layer TKE may act to weaken Rossiter modal structures. The shift in Rossiter modal frequencies may be due to the interaction of these mechanisms causing a change in α, and an acceleration of the freestream velocity due to the presence of the ramps ($f_m \propto U_\infty$).

Like the BC, the CS cavity shows a similar shift in Rossiter frequencies, possibly also due to acceleration of the freestream velocity. The CS cavity has larger modal amplitudes than the BC configuration. This may be associated with a large portion of the mixing layer positioned at nearly the same vertical location as the cavity trailing edge (Fig. 9g-i). The BC and CS cavities exhibited the large values of TKE spread throughout the cavity. It is expected that these increased levels of TKE should increase broadband fluctuations within these cavities.[22]

The ST cavity behaves similarly to the center scoop, although it appears to have a thinner mixing layer and a reduction in turbulent fluctuations within the cavity (Fig. 9j-l), resulting in a reduction of broadband fluctuations.[22] Referring to Fig. 12, the presence of the tooth increases the amplitude of the second Rossiter mode. As the tooth creates an overhang in the cavity, it is possible that this results in creation of a Helmholtz resonator. The Helmholtz frequency of the cavity may therefore further excite the second Rossiter mode, resulting in an increase in the modal amplitude. A simple model for providing a crude estimate of the Helmholtz frequency (f_H) of a resonance chamber is given by:

$$f_H = \frac{a}{2\pi}\sqrt{\frac{A_c}{\forall l}} \tag{2}$$

where a is the speed of sound, A_c is the cross-sectional area of the cavity inlet, $\forall$ is the total cavity volume, and l is the length of the throat. Using this Eq. (2), f_H was estimated as $\sim$ 1400 Hz, which is not far from the second Rossiter mode of the ST cavity, as shown in Fig. 12.

IV. Conclusions

SPIV was used to make volumetric measurements of the flows within four finite-span cavities of varying geometries in order to study the influence of edge effects. The cavities were studied within a transonic freestream at $M_\infty = 0.8$. The geometries investigated included a simple rectangular cavity (SR, $L/D = 7$, $b/L = 0.5$), a cavity with leading edge and side ramps (BC), a cavity with a centered scoop cut-out within the leading edge ramp (CS), and one with the scoop and a jagged leading edge protrusion (ST). Using the volumetric data obtained through this method, a number of conclusions were drawn based regarding the cavities tested:

(1) The reconstructed fluid volumes were able to illuminate a number of three-dimensionalities associated with each cavity. Flow separation along the side edge of the SR cavity resulted in the formation of a streamwise-oriented spillage vortex, which subsequently induced the formation of a secondary, counter-rotating vortical structure closer to the centerline of the cavity. These two structures induced mixing between the high-momentum freestream and the low-speed flow within the cavity, creating a localized region of accelerated flow roughly halfway between the cavity side wall and centerline. This resulted in a spanwise-waviness within the SR cavity flow field, whose amplitude grows with increasing streamwise distance.

(2) Through the addition of the leading edge and side ramps, the flow within the BC cavity was markedly

different from the SR cavity, with the noticeable absence of spillage vortices. The leading edge ramp elevated the mixing layer above the cavity floor. This resulted in lower velocity flow impingement on the rear wall of the cavity, which should create weaker Rossiter modal structures. In addition, increased TKE within the BC cavity flow field should further dissipate energy associated with these structures, resulting in a reduction in Rossiter amplitudes. Convective acceleration about the ramps and mixing layer of this cavity also accelerated the freestream velocity, causing the Rossiter modal frequencies to increase in comparison to the SR cavity.

(3) The center scoop cut-out appears to provide for a location for the formation of streamwise vorticity upstream of the leading edge. This restores the spillage and induced streamwise vortices, while also dropping the mixing layer at centerline. The mixing layer gradually increases vertically in height, following the morphology of the scoop. As a result of the presence of the scoop and the acceleration of flow about the ramps, the CS cavity showed a shift in the Rossiter frequencies similar to the BC cavity, but with increased amplitudes. Due to the presence of the counter-rotating vortex pair, a slight developing waviness, similar to that seen in the SR cavity was also observed. The CS cavity exhibited large amounts of TKE throughout the cavity, similar to the BC configuration, but increased in magnitude, causing increased broadband fluctuations.

(4) The ST cavity showed a similar spanwise trend as the center scoop, although with a greatly weakened spillage vortex. The presence of the overhanging tooth created a single streamwise vortex along the centerline, and partially enclosed flow. Compared to the CS cavity, the results showed a decrease in TKE and thinner mixing layer. Possible due to the influence of the overhang, this cavity showed a large increase in amplitude for Rossiter mode 2, possibly due to excitation by the Helmholtz frequency of the cavity.

More recent results by Casper et al.[31] have begun to examine the unsteady influence of these geometries using high-speed pressure sensitive paint PSP along the floor of each cavity. Future work will look to make use of the PSP, volumetric measurements presented here, and high-speed time-resolved PIV using a pulse-burst laser in order to provide further insight into changes introduced to the Rossiter modes by the complex geometries.

Acknowledgments

The authors would like to thank Thomas W. Grasser for his help in the designing of the experimental hardware. In addition, the authors would like to thank Dr. Katya M. Casper for compiling and producing Fig. 12, power spectral density measurements of the different cavity configurations.

This work is supported by Sandia National Laboratories and the United States Department of Energy. Sandia National Laboratories is a multi-program laboratory managed and operated by the Sandia Corporation, a wholly owned subsidiary of the Lockheed Martin Corporation, for the U.S. Department of Energy's National Nuclear Security Administration, under contract DE-AC04-94AL85000.

References

[1]Tracy, M.B., and Plentovich, E.B., "Cavity unsteady-pressure measurements at subsonic and transonic speeds," NASA Technical Paper 3669, Dec. 1997.

[2]Ahuja, K.K., and Mendoza, J., "Effects of cavity dimensions, boundary layer, and temperature on cavity noise with emphasis on benchmark data to validate computational aeroacoustic codes," NASA CR-4653, April 1995.

[3]Disimile, P.J., Toy, N., and Savory, E., "Effect of planform aspect ratio on flow oscillations in rectangular cavities," *Transactions of the ASME*, Vol. 122, 2000, pp. 32-38.

[4]Woo, C., Kim, J., and Lee, K., "Three-dimensional effects of supersonic cavity flow due to the variation of cavity aspect and width ratios," *Journal of Mechanical Science and Technology*, Vol. 22, 2008, pp. 590-598.
doi: 10.1007/s12206-007-1103-9.

[5]Hein, S., Koch, W., and Schoberl, J., "Acoustic resonances in a 2D high lift configuration and 3D open-cavity," AIAA Paper 2005-2867, May 2005.
doi: 10.2514/6.2005-2867.

[6]Brès, G.A., and Colonius, T., "Three-dimensional instabilities in compressible flow over open cavities," *Journal of Fluid Mechanics*, Vol. 599, 2008, pp. 309-339.
doi: 10.1017/S0022112007009925.

[7]de Vicente, J., Basley, J., Meseguer-Garrido, F., Soria, J., and Theofilis, V., "Three-dimensional instabilities over a rectangular open cavity: from linear stability analysis to experimentation," *Journal of Fluid Mechanics*, Vol. 748, 2014, pp. 189-220.
doi: 10.1017/jfm.2014.126.

[8]George, B., Ukeiley, L., Cattafesta, L.N., and Taira, K., "Control of three-dimensional cavity flow using leading-edge slot blowing," AIAA Paper 2015-1059, Jan. 2015.
doi: 10.2514/6.2015-1059

[9]Sun, Y., Zhang, Y., Taira, K., Cattafesta, L.N., George, B., and Ukeiley, L.S., "Width and sidewall effects on high speed cavity flows," AIAA Paper 2016-1343-1, Jan. 2016.
doi: 10.2514/6.2016-1343-1

[10]Dudley, J.G., and Ukeiley, L., "Detached eddy simulation of a supersonic cavity flow with and without passive flow control," AIAA Paper 2011-3844, June 2011.
doi: 10.2514/6.2011-3844.

[11]Beresh, S.J., Wagner, J.L., Pruett, B.O.M., Henfling, J.F., and Spillers, R.W., "Supersonic flow over a finite-width rectangular cavity," *AIAA Journal*, Vol. 53, No. 2, 2015, pp. 296-310; also AIAA Paper 2013-0389, Jan. 2013.
doi: 10.2514/1.J053097.

[12]Beresh, S.J., Wagner, J.L., Henfling, J.F., Spillers, R.W., Pruett, B.O.M., "Width effects in transonic flow over a rectangular cavity," *AIAA Journal*, Vol. 53, No. 12, 2015, pp. 3831-3834.
doi: 10.2514/1.J054362.

[13]Ohmichi, Y., and Suzuki, K., "Flow structure and heating augmentation around finite-width cavity in hypersonic flow," *AIAA Journal*, Vol. 52, No. 8, 2014, pp. 296-310; also AIAA Paper 2011-3966, June 2011.
doi: 10.2514/1.J052647.

[14]Arunajatesan, S., Barone, M.F., Wagner, J.L., Casper, K.M., and Beresh, S.J., "Joint experimental/computational investigation into effects of finite width on transonic cavity flow," AIAA Paper 2014-3027, June 2014.
doi: 10.2514/6.2014-3027.

[15]Crook, S.D., Lau, T.C.W., and Kelso, R.M., "Three-dimensional flow within shallow, narrow cavities," *Journal of Fluid Mechanics*, Vol. 735, 2013, pp. 587-612.
doi: 10.1017/jfm.2013.519.

[16]Wagner, J.L., Casper, K.M., Beresh, S.J., Hunter, P.S., Spillers, R.W., Henfling, J.F., and Mayes, R.L., "Fluid-structure interactions in compressible cavity flows," *Physics of Fluids*, Vol. 27, 2015, pp. 1-20.
doi: 10.1063/1.4922021.

[17]Coley, C.J., and Lofthouse, A.J., "Correlation of weapon bay resonance and store unsteady force and moment loading," AIAA Paper 2012-0415, Jan. 2012.

[18]Murray, N.E., and Jansen, B.J., "Effect of door configuration on cavity flow modulation process," *AIAA Journal*, Vol. 50, No. 12, 2012, pp. 2932-2937.
doi: 10.2514/1.J051650.

[19]Panickar M.B., Murray, N.E., Jansen, B.J., and Joachim, M.P., "Reduction of noise generated by a half-open weapons bay," *Journal of Aircraft*, Vol. 50, No. 3, 2013, pp. 716-724.
doi: 10.2514/1.C031747.

[20]Oza, U., Hu, Z., and Zhang, X., "Effect of cavity flow on landing gear aerodynamic loads," AIAA Paper 2016-2288, June 2015.
doi: 10.2514/6.2015-2288

[21]Sheta, E.F., Harris, R.E., Luke, E., George, B., and Ukeiley, L., "Loads and acoustics prediction on deployed weapons bay doors," AIAA Paper 2015-3018, June 2015.
doi: 10.2514/6.2015-3018.

[22]Casper, K.M., Wagner, J.L., Beresh, S.J., Henfling, J.F., Spillers, R.W., and Pruett, B.O.M., "Complex geometry effects on cavity resonance,"*AIAA Journal*, published online 7 Sept. 2015; also AIAA Paper 2015-1291, Jan. 2015.
doi: 10.2514/1.J054273.

[23]DeMauro, E.P., Beresh, S.J., Wagner, J.L., Henfling, J.F., and Spillers, R.W., "Volumetric measurement of transonic cavity flow using stereoscopic particle image velocimetry," AIAA Paper 2016-2076, Jan. 2016.
doi: 10.2514/6.2016-2076

[24]Wagner, J.L., Casper, K.M., Beresh, S.J., Henfling, J.F., Spillers, R.W., Pruett, B.O., "Mitigation of wind tunnel wall interactions in subsonic cavity flows," *Experiments in Fluids*, 2015, pp. 56-59.
doi: 10.1007/s00348-015-1924-8.

[25]Haigermoser, C., Scarano, F., Onorato, M., "Investigation of the flow in a rectangular cavity using tomographic and time-resolved PIV," 26th International Congress of the Aeronautical Sciences, Paper ICAS 2008-3.2.2, Sept. 2008.

[26]Haigermoser, C., Scarano, F., Onorato, M., "Investigation of the flow in a circular cavity using stereo and tomographic particle image velocimetry," *Experiments in Fluids*, Vol. 46, 2009, pp. 517-526.
doi: 10.1007/s00348-008-0577-2.

[27]Beresh, S.J., Wagner, J.L., DeMauro, E.P., Henfling, J.F., and Spillers, R.W., "Resonance characteristics of transonic flow over a rectangular cavity using pulse-burst PIV," AIAA Paper 2016-1344, Jan. 2016.
doi: 10.2514/6.2016-1344

[28]Wagner, J.L., Beresh, S.J., Casper, K.M., DeMauro, E.P., Arunajatesan, S., Henfling, J.F., and Spillers, R.W., "Relationship between transonic cavity tones and flowfield dynamics using pulse-burst PIV," AIAA Paper 2016-1345, Jan. 2016.
doi: 10.2514/6.2016-1345

[29]Rossiter, J.E., "Wind-tunnel experiments on the flow over rectangular cavities at subsonic and transonic speeds," Aeronautical Research Council Reports and Memoranda No. 3438, Oct. 1964.

[30]Heller, H.H., and Bliss, D.B., "The physical mechanism of flow-induced pressure fluctuations in cavities and concepts for their suppression," AIAA Paper 75-491, March 1975.
doi: 10.2514/6.1975-491.

[31]Casper, K.M., Wagner, J.L., Beresh, S.J., Spillers, R.W., and Henfling, J.F., "Unsteady pressure sensitive paint measurements of resonance properties in complex cavities," to be presented at the 46th AIAA Fluid Dynamics Conference, June 2016.